Analytical modeling of surface roughness in precision grinding of particle reinforced metal matrix composites considering nanomechanical response of material

Zhang, Z., Yao, P., Wang, J., Huang, C., Cai, R. & Zhu, H.

Original citation & hyperlink:
Zhang, Z, Yao, P, Wang, J, Huang, C, Cai, R & Zhu, H 2019, 'Analytical modeling of surface roughness in precision grinding of particle reinforced metal matrix composites considering nanomechanical response of material' International Journal of Mechanical Sciences, vol. 157-158, pp. 243-253
https://dx.doi.org/10.1016/j.ijmecsci.2019.04.047

DOI 10.1016/j.ijmecsci.2019.04.047
ISSN 0020-7403

Publisher: Elsevier

Analytical Modelling of Surface Roughness in Precision Grinding of Particle Reinforced Metal Matrix Composites Considering Nanomechanical Response of Material

Zhenzhong Zhang , Peng Yao , Jun Wang , Chuanzhen Huang , Rui Cai , Hongtao Zhu

PII: S0020-7403(18)33699-3
DOI: https://doi.org/10.1016/j.ijmecsci.2019.04.047
Reference: MS 4894

To appear in: *International Journal of Mechanical Sciences*

Received date: 11 November 2018
Revised date: 31 March 2019
Accepted date: 22 April 2019

Please cite this article as: Zhenzhong Zhang , Peng Yao , Jun Wang , Chuanzhen Huang , Rui Cai , Hongtao Zhu , Analytical Modelling of Surface Roughness in Precision Grinding of Particle Reinforced Metal Matrix Composites Considering Nanomechanical Response of Material, *International Journal of Mechanical Sciences* (2019), doi: https://doi.org/10.1016/j.ijmecsci.2019.04.047

Highlights

- A mathematical surface roughness prediction model of ground PRMMCs considering different removal mechanisms of matrix and reinforcements was proposed
- The measured modulus and hardness of TiC particle with its surrounding steel matrix is reduced from that of TiC itself due to the secondary indentation
- The theoretical predictions are well consistent with experimental data for GT35

Analytical Modelling of Surface Roughness in Precision Grinding of Particle Reinforced Metal Matrix Composites Considering Nanomechanical Response of Material

Zhenzhong Zhang[a,b], Peng Yao[a,b*], Jun Wang[c], Chuanzhen Huang[a,b], Rui Cai[d], Hongtao Zhu[a,b]

[a]*Center for Advanced Jet Engineering Technologies (CaJET), School of Mechanical Engineering, Shandong University, Jinan, Shandong 250061, China*

[b]*Key Laboratory of High Efficiency and Clean Mechanical Manufacture, Shandong University, Ministry of Education, Jinan, Shandong 250061, PR China*

[c]*School of Mechanical and Manufacturing Engineering, The University of New South Wales (UNSW), Sydney, NSW 2052, Australia*

[d] *School of Mechanical, Aerospace and Automotive Engineering, Coventry University, 3 Gulson Road, CV1 2JH, Coventry, UK*

Abstract

Grinding is usually applied for particle reinforced metal matrix composites (PRMMCs) to achieve high ground surface quality. However, the surface quality especially surface roughness is difficult to predict theoretically due to different mechanical properties of two or more phases inside the PRMMCs. In this study, an analytical model of the surface roughness of ground PRMMCs is developed based on an undeformed chip thickness model with Rayleigh probability distribution by considering the different removal mechanism of metal matrix and reinforcement particles in grinding. GT35, a typical kind of steel based metal matrix composite reinforced with TiC particles is investigated as an example.

* Corresponding authors:

Peng Yao, Center for Advanced Jet Engineering Technologies (CaJET), School of Mechanical Engineering, Shandong University, Jinan, Shandong 250061, China. Email: yaopeng@sdu.edu.cn;

Nanoindentation experiments are employed for the investigation of nanomechanical properties and cracking behavior of GT35 and the nanoindentation results are integrated in the model. Single factor surface grinding experiments of GT35 are also carried out to understand the material removal mechanism of GT35 and validate this novel surface roughness prediction model. The predicted surface roughness from this model shows good agreement with the experimental results.

Keywords: PRMMCs; Precision grinding; Surface roughness; Nanoindentation.

Nomenclature

A	shaded area	v_d	cup wheel speed
C_d	dynamic grit density	v_s	wheel speed
E	elastic modulus	v_ω	work-piece speed
h	undeformed chip thickness	y_{cl}	position of the center-line
H	hardness	α	geometry factor of the indenter
K_c	fracture toughness.	α_0	top angle of the indentor
K_0	affecting coefficient of the coolant	Δ	grinding depth
K_{Id}	dynamic fracture toughness	Δ_d	dressing depth
l_c	contact length	θ	semi-included angle of grain
p	probability	μ	material parameter determined by elastic recovery
R_a	arithmetic mean surface roughness	σ	parameter of probability density function
v	poisson's ratio	σ_y	yield stress
		φ	volume fraction of reinforcement particles in metal matrix composites

1 Introduction

Particle reinforced metal matrix composites (PRMMCs), such as SiCp/Al, Al_2O_3/Al, SiCp/Mg and TiC/Fe, etc., are a mixture of two or more materials, one being a metal or alloy, the other being a ceramic or another organic compound [1,2]. They are important engineering materials combining excellent ductility of metals and high stiffness and strength of hard particles together [3]. GT35 discussed in this paper is a steel-based metal matrix composite, also known as steel bonded carbide. It is reinforced with TiC ceramic particles with mass fraction of 35%TiC. Due to its low friction coefficient, high thermo-stability, wear resistance, and corrosion resistance, GT35 is being widely used in many engineering components such as tools, dies, precision astronautic parts, etc. with requirements of high precision and high surface quality. However, this material is very difficult to cut due to several reasons: Firstly, the hardness of quenched GT35 reach HRC70, which leads to high cutting force, cutting temperature, tool wear and poor workpiece surface quality. Secondly, the properties of the two phases are very different [4] in terms of strength and modulus, which leads to high machining vibration and ground surface defects. As a result, precision grinding is commonly implemented to machine this difficult to cut material.

It is well known that machining hard-brittle materials in ductile mode could be realized if the maximum grit depth of cut is controlled below the depth of cut in brittle-ductile transition [5], or the material is ground in brittle mode with cracks and subsurface damages. Many efforts have been put to achieve ductile grinding for hard-brittle materials, e.g. grinding in high-speed [6], with ultra-fine grits wheels [7] or in dry conditions [8]. In grinding the different mechanical properties of the two phases of PRMMCs lead to diverse material removal modes including the ductile mode, brittle mode and hybrid mode, which affect the final machined surface quality. Hung [9] applied ductile-regime machining in order to

enhance the surface quality of PRMMCs. In his study, the ductile mode machining of matrix was achieved, however the particles were fractured and the surface quality was dramatically declined accordingly. Yu et al. [10] investigated the machining characteristics of SiCp/Al composites under ELID grinding conditions. The results indicated that SiC reinforcing particles were removed in ductile regime. As a result, the high integrity surface of PRMMCs was obtained. Xi et al. [11] explored the effect of reinforcement phase on the surface roughness during high speed grinding of TiCp/Ti-6Al-4V. It was concluded that the removal mode of the reinforcement phase highly correlates with the surface quality. Liu et al. [12] studied the influence of the undeformed chip thickness on the formation of ground surface defects in the grinding of PRMMCs. It was concluded that the undeformed chip thickness plays a crucial role in the removal of reinforcement particle-the particle crushing increases with the increase of the undeformed chip thickness. Hence, the prediction of surface quality of PRMMCs after precision grinding would be more complex than that of single-phase materials due to the additional reinforcement phase.

Many studies on the surface roughness prediction model for composite material using different methods have been carried out [13-17] in order to optimize processing parameters. Basheer et al. [13] presented an artificial neural network (ANN)-based model to predict the surface roughness of Al/SiCp composite in precision machining. The ANN model showed good prediction accuracy with the correlation coefficient of 0.977 and mean absolute error of 10.4%. Kwak and Kim [14] proposed a second-order response surface model for predicting roughness in grinding of aluminum matrix composites. The variation trend of the surface roughness was easily get through the three-dimensional plot of the developed response surface. Chandrasekaran [15] proposed an ANN model to study the effect of process parameters in the cylindrical grinding process of PRMMCs. In his model, wheel speed, feed,

workpiece velocity and grinding depth are used as inputs for the neural network to assess the surface roughness of PRMMCs. The analytic results of variance (ANOVA) showed that wheel speed was the main parameter affecting the surface roughness. However, there are limitations for the above models. Firstly, the effect of material and wheel characterization were not considered in these models so far. Secondly, the above models are limited to the processing conditions where the grinding experiments were conducted, and need to be extended to other scenarios.

Meanwhile, numerous theoretical models have been introduced to overcome the limitations of the empirical models. Hecker and Liang [16]applied a theoretical model for predicting surface roughness based on the unformed chip thickness model in cylindrical grinding. The model analyses the relations of the ground surface integrity with the wheel characteristics, the workpiece properties and the grinding parameters. Agarwal and Rao [17]took a similar technique to predict the surface roughness in ceramic grinding. The model was validated by the results of grinding SiC, but it was developed without considering the effects of the ductile and brittle regime material-removing characteristic of ceramic grinding. In addition, the model is not related to the actual ground surface morphology, and it is only valid for coarse grinding of ceramics when the materials are completely removed in the brittle mode. In general, few analytical or theoretical models have been applied in the prediction of surface roughness of PRMMCs.

In this paper, an analytical model based on the undeformed chip thickness model is developed to predict the ground surface roughness of PRMMCs considering different material removal mechanisms of matrix and reinforcement particles. Nanoindentation is a reliable tool for investigating nanomechanical properties of materials [18] and mechanical

responds of the workpiece in precision grinding. Therefore, nanoindentation experiments are conducted to investigate the nanomechanical properties and cracking behaviors of two phases in GT35. The ground surfaces are observed to understand the material removal mechanism of GT35 in grinding. The theoretical surface roughness prediction model is verified by comparing its prediction results with the corresponding experimental results of ground GT35.

2 Analytical model of surface roughness in PRMMCs grinding

2.1 The chip thickness and surface profile

The ground profile of workpiece is generated by the grooves cut by abrasive grains. The distribution of the undeformed chip thickness, *h*, or penetration depth of abrasive grain can be expressed with Rayleigh probabilities [19], as

$$f(h) = \begin{cases} (h/\sigma^2)e^{-h^2/2\sigma^2} & h \geq 0 \\ 0 & h < 0 \end{cases} \quad (1)$$

with the expectation and standard deviation represented as

$$E(h) = \sqrt{\pi/2}\sigma \quad (2)$$

$$sd(h) = \sqrt{0.429}\sigma \quad (3)$$

The parameter σ, which defines the probability density function, can be calculated as:

$$\sigma = \sqrt{\frac{\Delta \cdot v_\omega}{2v_s \cdot C_d} \frac{1}{l_c \cdot \tan\theta}} \quad (4)$$

where Δ is the grinding depth, v_ω the workpiece speed, v_s the wheel speed, C_d the dynamic grit density, l_c the contact length and θ the semi-included angle of grain. In this study, θ=45°.

Figure 1 shows a probability distribution of undeformed chip thickness or penetration depth of abrasive grain. The probabilities of the undeformed chip thickness include two parts

the probability for material removal dominated by the ductile flow for $h < h_{cr}$ or the probability for material removal dominated by brittle fracture.

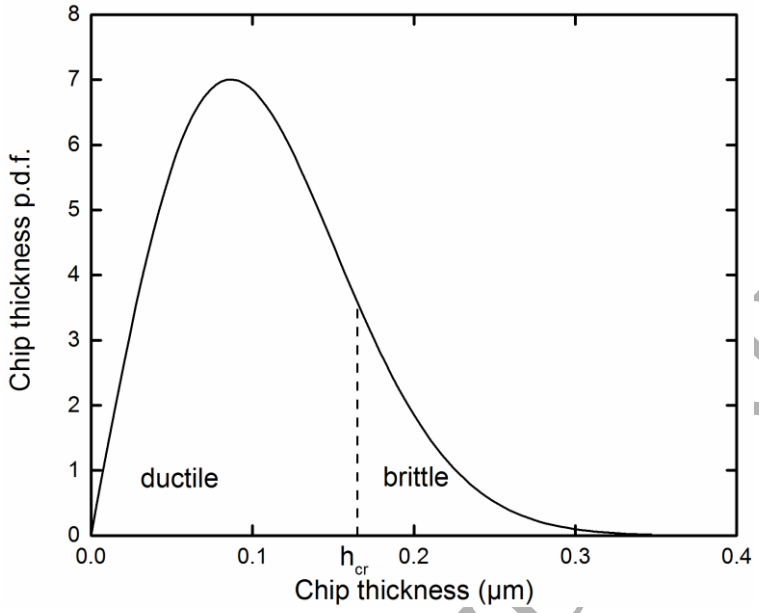

Fig. 1. Probability density function of undeformed chip thickness [19]

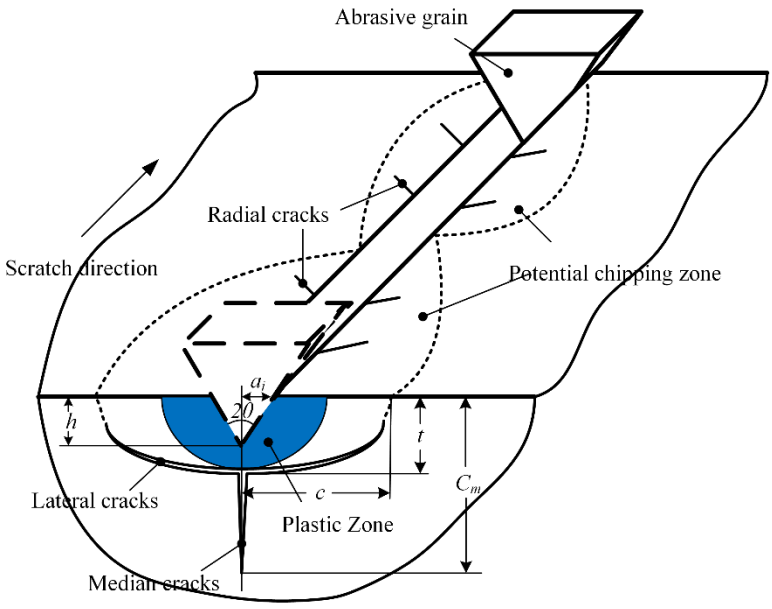

Fig. 2. Typical crack systems in brittle material induced by abrasive scratching process[20]

Regarding the surface generated in grinding of PRMMCs with two phases, the profile generated by the ductile mode can be represented by traces ploughed by abrasive grains, and the profile generated by the brittle mode can be represented by the lateral crack size c and the plastic zone depth t [20]. As shown in Fig. 2, there are two main types of cracks in the plastic zone when scratching brittle materials, i.e., radial cracks and lateral cracks. The relation between the penetration depth h and the lateral cracking depth t is defined as [21]:

$$t = K_L h \cdot tan\theta \tag{5}$$

where

$$K_L = [\frac{3(1-2\nu)}{5-4\nu} + \frac{2\sqrt{3}}{\pi(5-4\nu)}\frac{E}{\sigma_y}cot\,\theta]^{1/2} \tag{6}$$

where ν is the Poisson ratio, ν is 0.19 for TiC; E is the elastic modulus and σ_y is the Yield stress.

The median crack length is defined as the functional relation of material attributes, conical shape is of grain tips, and depth of grain engagement [22].

$$c_m = 0.206\frac{(E\cdot H)^{1/3}}{(K_C\cdot\mu)^{2/3}}(cot\theta)^{4/9}(h\cdot tan\theta)^{4/3} \tag{7}$$

where K_c is the fracture toughness and μ is the coefficient of elastic recovery. For TiC, μ is 0.35.

The length of the lateral crack c is one-seventh of the median crack c_m [23].

$$c = 1/7 c_m \tag{8}$$

Therefore, the relationship between the penetration depth h and the lateral cracking size c is:

$$c = K_M(h\cdot tan\theta)^{4/3} \tag{9}$$

$$K_M = \frac{0.206}{7}\frac{(E\cdot H)^{1/3}}{(K_C\cdot\mu)^{2/3}}(cot\theta)^{4/9} \tag{10}$$

2.2 Surface roughness modeling

The relation between the reinforcement particle size and the surface roughness of the composites is shown in Fig. 3(a) and Fig.3(b). Fig. 3(a) shows Case 1 when the tool nose radius is larger than the size of reinforcement particles, which occurs in the conventional cutting of composites. The surface roughness depends on the profile of cutting tool rather than removal mode of particles. Case 2 in Fig. 3(b) occurs during precision grinding of composites when the tool nose radius is smaller than the size of the reinforcement particles. In this case, the impact of the removal mode of reinforcement particles cannot be neglected on the surface roughness generation of the composites.

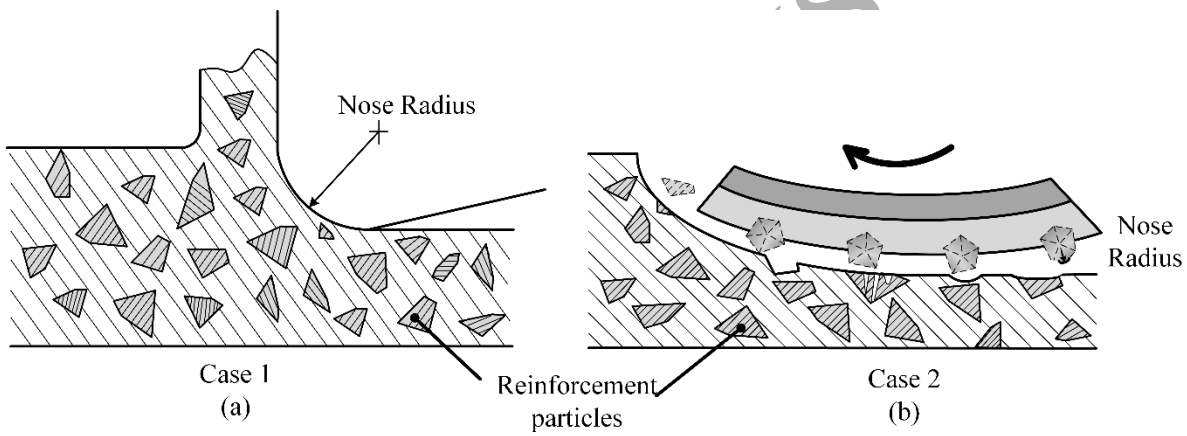

Fig. 3. Models for the effects of reinforcement particles on surface roughness

The flowchart for the modelling procedure is shown in Fig. 4, when PRMMCs are ground, the two phases of the PRMMCs may be removed in different removal modes. Hence, the modelling of surface roughness falls into two different sub models. In grinding reinforcement particles, as both the brittle mode and ductile mode exist, the model takes into account lateral fracture crack and plastic striations. In grinding matrix (steel), the removal mode of the ground surface is mainly the ductile mode. Based on the probabilities of the chip thickness and grinding parameters, the surface roughness model is built. Stages I-V in Fig. 4

correspond to sections I-V in Fig. 5. The surface roughness of PRMMCs can be represented as:

$$R_a = \varphi R_{ar} + (1 - \varphi) R_{am} \tag{11}$$

where φ is the volume fraction of reinforcement particles in metal matrix composites, R_a is the surface roughness of PRMMCs, R_{ar} and R_{am} are the surface roughness values of reinforcement particles and matrix respectively.

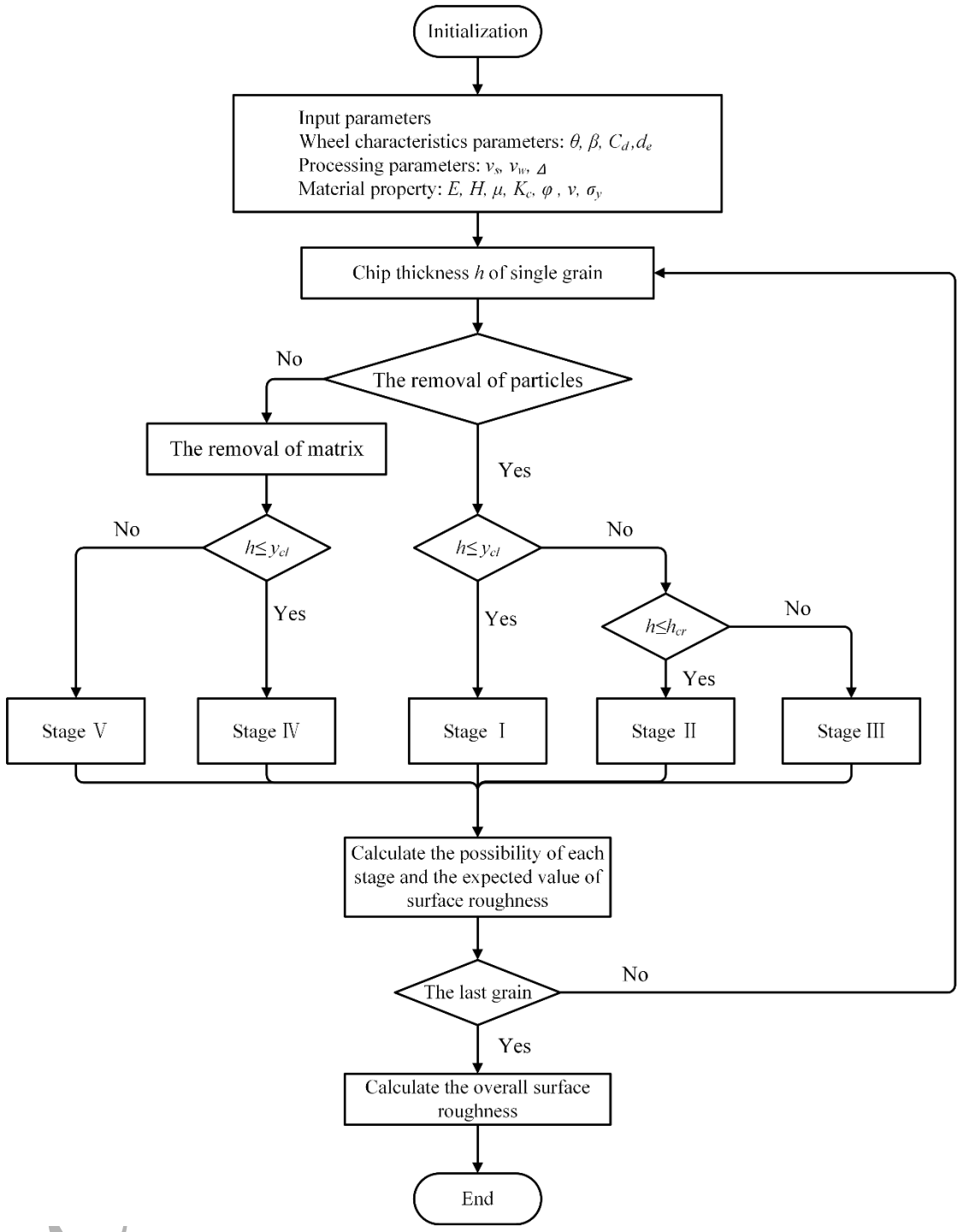

Fig. 4. Flowchart for modelling the surface roughness of ground PRMMCs

Based on the hypothesis of Hecker and Liang [16], different removal modes in the two phases of PRMMCs are considered. In addition, certain assumptions are proposed to simplify the model in this study as follows:

(1) Grooves are generated by material removal of reinforcement particles in two modes, one is the ductile mode, and the other is the brittle mode. In the ductile mode, grooves are represented by triangular shape from the chip thickness of the active grains as shown in sections I-II in Fig. 5. While in the brittle mode, grooves are represented by the lateral cracks triangles with length *2c* and depth *t*, as shown in section III in Fig. 5. Grooves generated in matrix are represented by the chip thickness of the active grains as shown in sections IV-V in Fig. 5.

(2) Grooves do not overlap each other.

(3) The predicted surface roughness is in a direction perpendicular to the feeding direction.

On the basis of these assumptions, the profile of the grooves generated by grains is illustrated in Fig. 5.

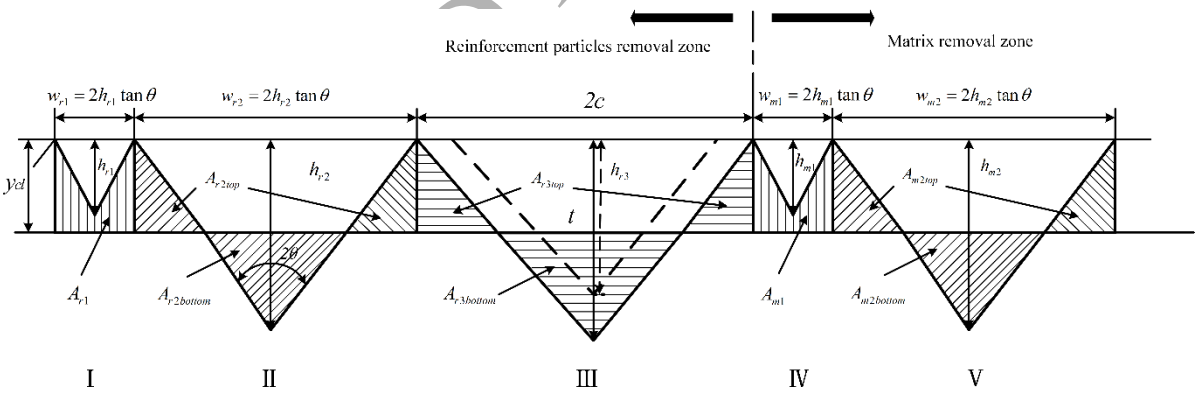

Fig. 5. Theoretical profile with grooves generated in ductile and brittle removal modes

The surface roughness Ra is the arithmetic mean of absolute contour height deviations from the mean plane within the assessed length. The formula is shown below:

$$R_a = \frac{1}{L}\int_0^L |y - y_{cl}|\, dl \tag{12}$$

where y_{cl} is the centre line of the assessed profile. The area above the centre line is equal to the area below it.

According to the definition of surface roughness,

$$p_{r1}E(A_{r1}) + p_{r2}E(A_{r2_{top}}) + p_{r3}E(A_{r3_{top}}) + p_{m1}E(A_{m1}) + p_{m2}E(A_{m2_{top}}) = p_{r2}E(A_{r2_{bottom}}) + p_{r3}E(A_{r3_{bottom}}) + p_{m2}E(A_{m2_{bottom}}) \quad (13)$$

where p_{r1} and p_{r2} are the probabilities of the penetration depth of abrasive grains, which are smaller and larger than y_{cl} respectively, but both are less than the critical value h_{cr}. p_{r3} is the probability of the penetration depth of abrasive grains, which is larger than the critical value h_{cr} in particle removal. p_{m1} and p_{m2} are the probabilities of the penetration depth of abrasive grains which is smaller and larger than y_{cl} in matrix removal. These probabilities are expressed as

$$p_{r1} = \varphi \int_0^{y_{cl}} f(h)\, dh \quad (14)$$

$$p_{r2} = \varphi \int_{y_{cl}}^{h_{cr}} f(h)\, dh \quad (15)$$

$$p_{r3} = \varphi \int_{h_{cr}}^{\infty} f(h)\, dh \quad (16)$$

$$p_{m1} = (1-\varphi) \int_0^{y_{cl}} f(h)\, dh \quad (17)$$

$$p_{m2} = (1-\varphi) \int_{y_{cl}}^{\infty} f(h)\, dh \quad (18)$$

where φ is the volume fraction of reinforcement particles in metal matrix composites.

During the removal of particles, the area above the centre line in section I is expressed as:

$$E(A_{r1}) = tan\theta\left[2y_{cl}E(h_{r1}) - E\left({h_{r1}}^2\right)\right] \quad (19)$$

where h_{r1} represents the penetration depth in grooves which is smaller than y_{cl}.

Similarly, the areas of the grooves with the penetration depth (h_{r2}) which is larger than y_{cl} but smaller than h_{cr} in section II are expressed as:

$$E(A_{r2_{top}}) = tan\theta {y_{cl}}^2 \quad (20)$$

$$E(A_{r2_{bottom}}) = tan\theta\left[E\left({h_{r2}}^2\right) - 2y_{cl}E(h_{r2}) + {y_{cl}}^2\right] \quad (21)$$

where $E(A_{r2_{top}})$ and $E(A_{r2_{bottom}})$are the areas above and below the centre line as shown in Fig. 5.

Moreover, the areas of the cracked grooves with the penetration depth (h_{r3}) which is larger than h_{cr} in section III are expressed as:

$$E(A_{r3_{top}}) = {y_{cl}}^2 E\left(\frac{c}{t}\right) \quad (22)$$

$$E(A_{r3_{bottom}}) = E(tc) - 2E(c)y_{cl} + {y_{cl}}^2 E\left(\frac{c}{t}\right) \quad (23)$$

where $E(A_{r3_{top}})$ and $E(A_{r3_{bottom}})$ are the areas above and below the centre line as indicated in Fig. 5.

During the removal of matrix, the area of grooves with the penetration depth (h_{m1}) which is smaller than y_{cl} in section IV is expressed as:

$$E(A_{m1}) = tan\theta\left[2y_{cl}E(h_{m1}) - E\left({h_{m1}}^2\right)\right] \quad (24)$$

Similarly, the areas of the grooves with the penetration depth (h_{m2}) which is larger than y_{cl} in section V are expressed as:

$$E(A_{m2_{top}}) = tan\theta {y_{cl}}^2 \quad (25)$$

$$E(A_{m2_{bottom}}) = tan\theta[E\left({h_{m2}}^2\right) - 2y_{cl}E(h_{m2}) + {y_{cl}}^2] \quad (26)$$

where $E(A_{m2_{top}})$ and $E(A_{m2_{bottom}})$ are the areas above and below the centre line.

In order to calculate the expectations, the distribution functions in each region for those conditions in section I-V are defined as follows:

$$f(h)_{r1} = \frac{f(h)}{\int_0^{y_{cl}} f(h)dh} \qquad 0 \le h < y_{cl} \quad (27)$$

$$f(h)_{r2} = \frac{f(h)}{\int_{y_{cl}}^{h_{cr}} f(h)dh} \qquad y_{cl} \le h < h_{cr} \quad (28)$$

$$f(h)_{r3} = \frac{f(h)}{\int_{h_{cr}}^{\infty} f(h)dh} \qquad h_{cr} \le h < \infty \quad (29)$$

$$f(h)_{m1} = \frac{f(h)}{\int_0^{y_{cl}} f(h)dh} \qquad 0 \le h < y_{cl} \tag{30}$$

$$f(h)_{m2} = \frac{f(h)}{\int_{y_{cl}}^{\infty} f(h)dh} \qquad y_{cl} \le h < \infty \tag{31}$$

Substitute Eqs. (5) and (9) to Eqs. (22) and (23). Then Eqs. from (14) to (31) are substituted into Eq. (13), the centre line y_{cl} can be derived as

$$2y_{cl} = \frac{2\sigma^2 + p_{r3}K_L K_M tan\theta^{4/3} \cdot E\left({h_{r3}}^{7/3}\right) - p_{r3}E\left({h_{r3}}^2\right)}{\sqrt{\pi/2}\sigma + p_{r3}K_M tan\theta^{1/3} \cdot E\left({h_{r3}}^{4/3}\right) - p_{r3}E(h_{r3})} \tag{32}$$

where

$$p_{r3} = \varphi \int_{h_{cr}}^{\infty} f(h)dh$$

$$= \varphi e^{-\frac{{h_{cr}}^2}{2\sigma^2}} \tag{33}$$

$$E(h_{r3}) = \frac{1}{\int_{h_{cr}}^{\infty} f(h)dh} \int_{h_{cr}}^{\infty} hf(h)\,dh$$

$$= \frac{1}{\int_{h_{cr}}^{\infty} f(h)dh} \left[\sqrt{\frac{\pi}{2}}\sigma + e^{-\frac{{h_{cr}}^2}{2\sigma^2}} h_{cr} - \sqrt{\frac{\pi}{2}}\sigma Erf\left(\frac{h_{cr}}{\sqrt{2\sigma^2}}\right)\right] \tag{34}$$

$$E\left({h_{r3}}^2\right) = \frac{1}{\int_{h_{cr}}^{\infty} f(h)dh} \int_{h_{cr}}^{\infty} h^2 f(h)\,dh$$

$$= \frac{1}{\int_{h_{cr}}^{\infty} f(h)dh} \left(2\sigma^2 + {h_{cr}}^2\right) e^{-\frac{{h_{cr}}^2}{2\sigma^2}} \tag{35}$$

$$E\left({h_{r3}}^{3/7}\right) = \frac{1}{\int_{h_{cr}}^{\infty} f(h)dh} \int_{h_{cr}}^{\infty} h^{3/7} f(h)\,dh$$

$$= \frac{1}{\int_{h_{cr}}^{\infty} f(h)dh} \left[\frac{7}{36}\Gamma\left(\frac{1}{6}, \frac{{h_{cr}}^2}{2\sigma^2}\right)(2\sigma^2)^{7/6} + {h_{cr}}^{1/7}({h_{cr}}^2 + \frac{7}{3}\sigma^2) e^{-\frac{{h_{cr}}^2}{2\sigma^2}}\right] \tag{36}$$

$$E\left({h_{r3}}^{4/3}\right) = \frac{1}{\int_{h_{cr}}^{\infty} f(h)dh} \int_{h_{cr}}^{\infty} h^{4/3} f(h)\,dh$$

$$= \frac{1}{\int_{h_{cr}}^{\infty} f(h)dh} \left[({h_{cr}}^2)^{2/3} \cdot e^{\frac{-{h_{cr}}^2}{2\sigma^2}} + \frac{2}{3} \cdot (2\sigma^2)^{2/3} \cdot \Gamma(\frac{2}{3}, \frac{{h_{cr}}^2}{2\sigma^2})\right] \tag{37}$$

Finally, the total expectations of the surface roughness of sections I-V can be calculated as:

$$E(R_a) = p_{r1}E(R_{ar1}) + p_{r2}E(R_{ar2}) + p_{r3}E(R_{ar3}) + p_{m1}E(R_{am1}) + p_{m2}E(R_{am2}) \tag{38}$$

$$E(R_{ar1}) = E\left(\frac{A_{r1}}{2h_{r1}tan\theta}\right) \tag{39}$$

$$E(R_{ar2}) = E\left(\frac{2A_{r2top}+A_{r2bottom}}{2h_{r2}tan\theta}\right) \quad (40)$$

$$E(R_{ar3}) = E\left(\frac{A_{r3top}+A_{r3bottom}}{2c}\right) \quad (41)$$

$$E(R_{am1}) = E\left(\frac{A_{m1}}{2h_{m1}tan\theta}\right) \quad (42)$$

$$E(R_{am2}). = E\left(\frac{2A_{m2top}+A_{m2bottom}}{2h_{m2}tan\theta}\right) \quad (43)$$

3 Experimental work

To study the nanomechanical properties of the two phases in GT35, the nanoindentation experiments were performed on a nanomechanical property testing platform Nanotest Vantange (Micro Materials Corporation). The experimental setup is illustrated in Fig. 6, and the detailed nanoindentation parameters are listed in Table 1. Before the experiments, the specimen was polished for removing the surface defect layer. The surface roughness Ra of the polished specimen was about 10 nm. In order to mark the indentation position on the surface, the workpiece surface was marked by laser shooting. To reveal the nanomechanical properties of steel matrix and TiC particles respectively, specific indentation locations were selected by observing with a microscope in situ, so that the indentor can be pressed on a specific phase. Four repetitive indentations were conducted for each indentation parameter at various locations. The morphologies of plastic deformation and cracks in the indentations were observed by scanning electron microscope (SEM). The load-displacement curves of the loading and unloading process were recorded for figuring out the hardness and modulus of TiC particles.

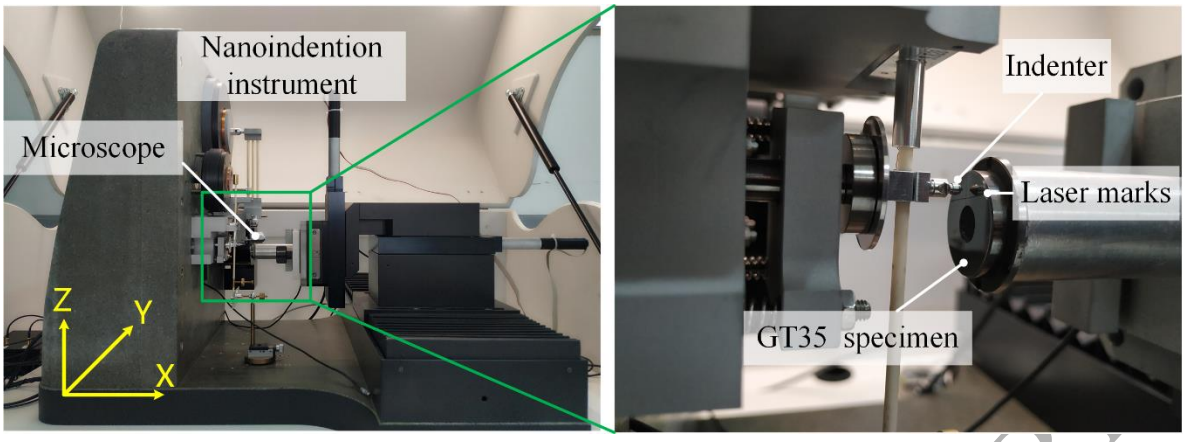

Fig. 6. Specimen and setup of nanoindentation experiments

Table 1 The indentation parameters.

Species	Load (mN)	Loading velocity (mN/s)	Unloading velocity (mN/s)	Dwell time (s)
TiC particles	5~300	2.5	2.5	10
Steel matrix	5~300	2.5	2.5	10

The set-up for the surface grinding experiments is shown in Fig. 7. The precision surface grinding experiments of GT35 workpiece were performed on an ultra-precision surface grinder (NAGASHIMA SEIKO NAS520-CNC) with a resin bond diamond wheel (#3000) with 200 mm diameter and 10 mm width. In order to improve the roundness and sharpness of the diamond grinding wheel, SiC cup wheel truer with grain size of 5 μm is applied to dress the diamond wheel before grinding experiments. The experimental details for dressing and grinding are shown in Table 2. A laser displacement sensor with 0.1 μm resolution (KEYENCE LK-G10) was used for on-machine measurement of the run-out of the conditioned grinding wheel. The envelope lines of measured grinding wheel profile were figured out. As shown in Fig. 8, the run-out of the wheel was conditioned precisely to 1 μm.

After dressing, the dynamic balance of the wheel was controlled to keep a wheel vibration under 20 nm during grinding.

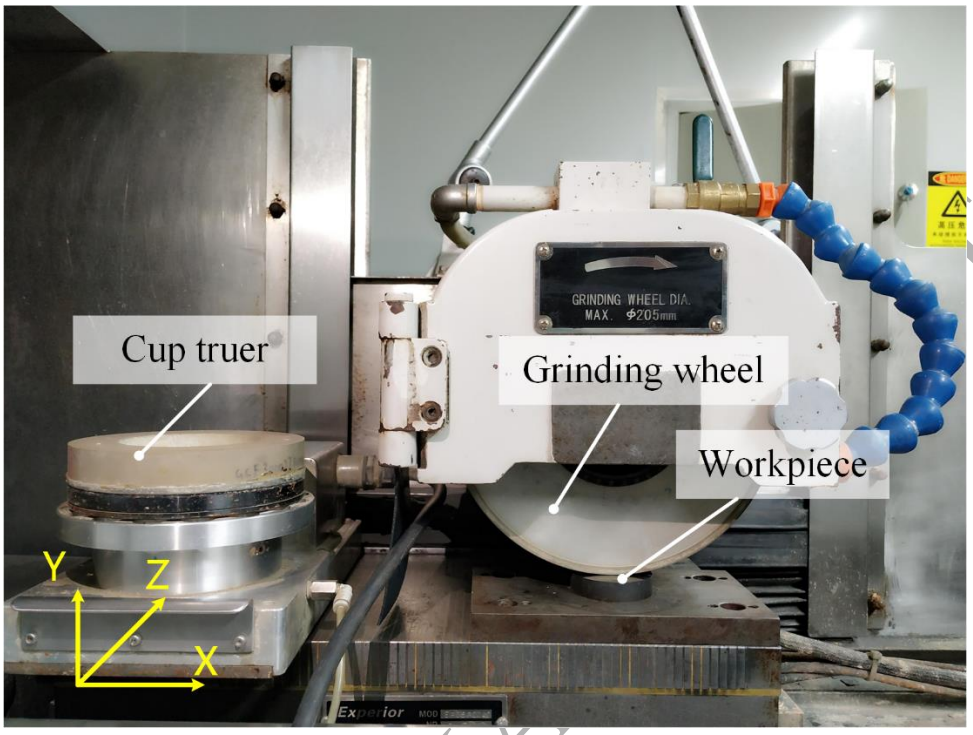

Fig. 7. Set-up for grinding experiments

Table 2 Experimental conditions.

Machine tool	NAGASHIMA SEIKO NAS520-CNC
Workpiece material	GT35
Grinding mode	Plunge surface grinding
Grinding wheel	#3000 Resin bonded diamond wheel
Cooling conditions	5% water-soluble coolants SC25AC
Dresser	SiC cup wheel truer with grain size of 5 μm
Dressing parameters	
Wheel speed v_s (m/s)	5
Cup wheel speed v_d (m/s)	7
Dressing depth Δ_d (μm)	3

Worktable feed rate v_w (mm/min)	500

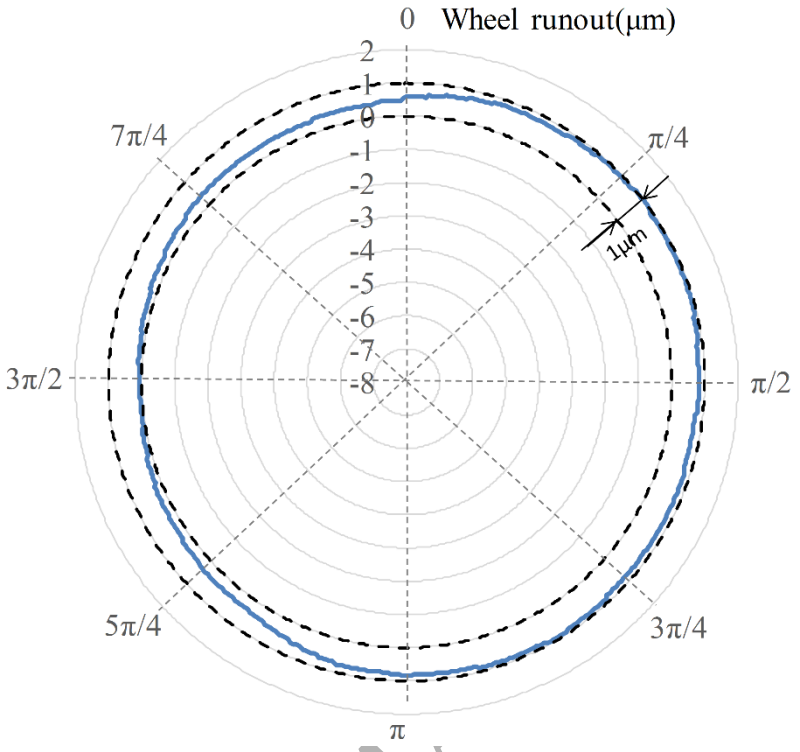

Fig. 8. Run-out of the precisely conditioned grinding wheel

Since the surface roughness model developed as Eq. (38) is based on the chip thickness model including the impact of grinding parameters such as the grinding depth, workpiece feed rate, and wheel speed. Hence, a series of single factor grinding experiments were carried out to analyse the effects of these parameters on the surface roughness. The grinding parameters including the grinding depth Δ (μm), workpiece feed rate v_w (m/s) and wheel speed v_s (m/s)) are listed in Table 3. The surface roughness of ground workpiece was measured with a laser scanning confocal microscope, KEYENCE VK-X200. Three times at random locations on the surface to calculate the mean values. The morphologies of the ground surface were examined with a scanning electron microscope (SEM) to analyse the material removal mechanisms of GT35.

Table 3 Grinding experimental parameters.

No.	Grinding depth Δ (μm)	Workpiece feed rate v_w (m/s)	Wheel speed v_s (m/s)
1	3	0.226	10
2	3	0.226	15
3	3	0.226	20
4	3	0.226	25
5	3	0.113	15
6	3	0.170	15
7	3	0.226	15
8	3	0.283	15
9	2	0.226	15
10	3	0.226	15
11	4	0.226	15
12	5	0.226	15

4 Results and Discussion

4.1 Nanomechanical properties of GT35

Fig. 9 shows the SEM images of nanoindentation topography under load from 5 mN to 300 mN of steel matrix. There are only regular indentation pits left by the indenter on the steel matrix surface, and no crack is observed on the surface of the matrix in all four indentations.

It can be concluded that ductile removal is obviously dominated in the grinding of the steel matrix. Fig. 10 shows the SEM images of Vickers indentation topography of TiC particles at various loads. The darker parts showing in the photographs are TiC particles. As shown in Fig. 10 (a)-(c), for the TiC particles, no crack emerges from the indentation until 100 mN. Lateral cracks occur under the loading of 200 mN in one indentation, as shown in Fig.10(d). It means that although TiC is hard and brittle, ductile grinding can be achieved when the maximum undeformed chip thickness is below the critical depth for the ductile-brittle transition. Besides lateral cracks, as shown in Figs. 10(e) and 10(f), the median and radial cracks are observed on the surface respectively. This shows that in nanoindentation of TiC particles, the critical load of crack initiation is 100~200 mN.

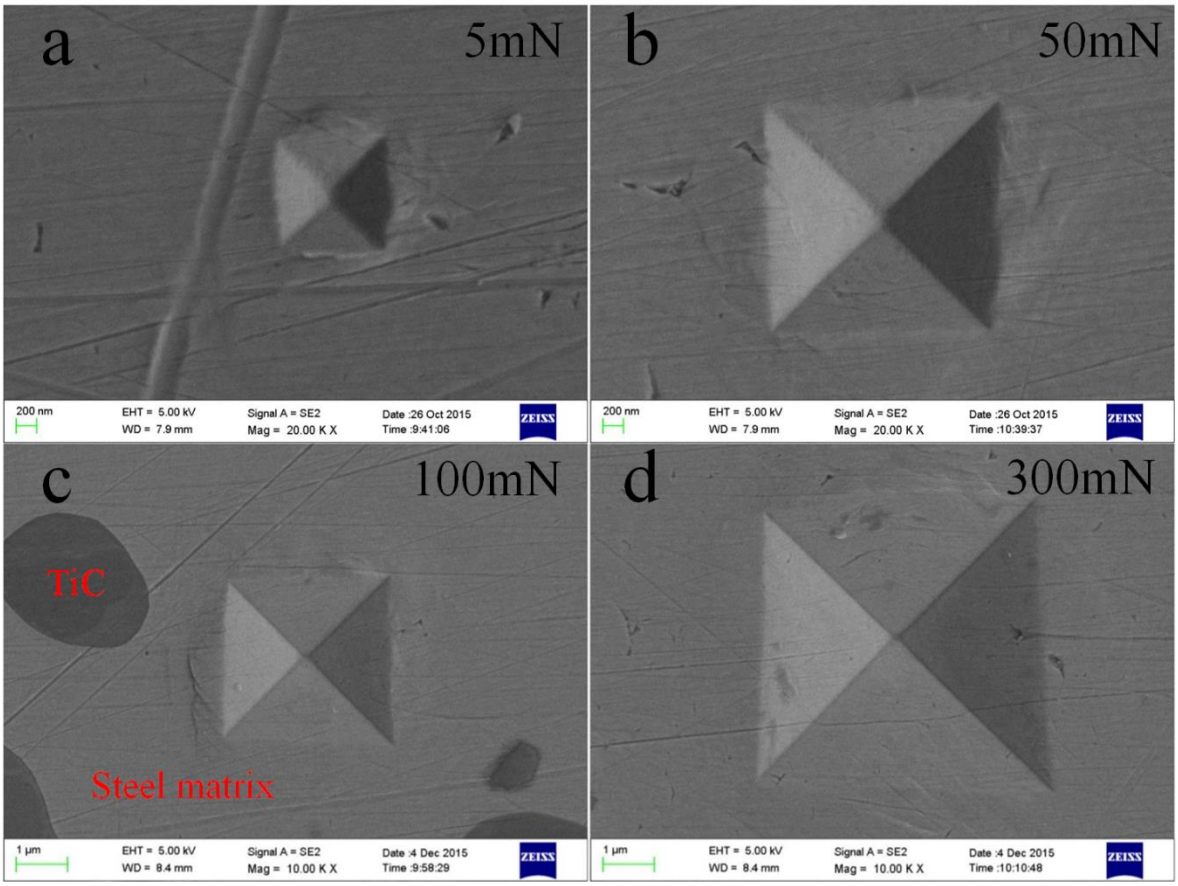

Fig. 9. SEM images of nanoindentation topography for steel matrix under different loads of. (a) 5 mN. (b) 50 mN. (c) 100 mN. (d) 300 mN.

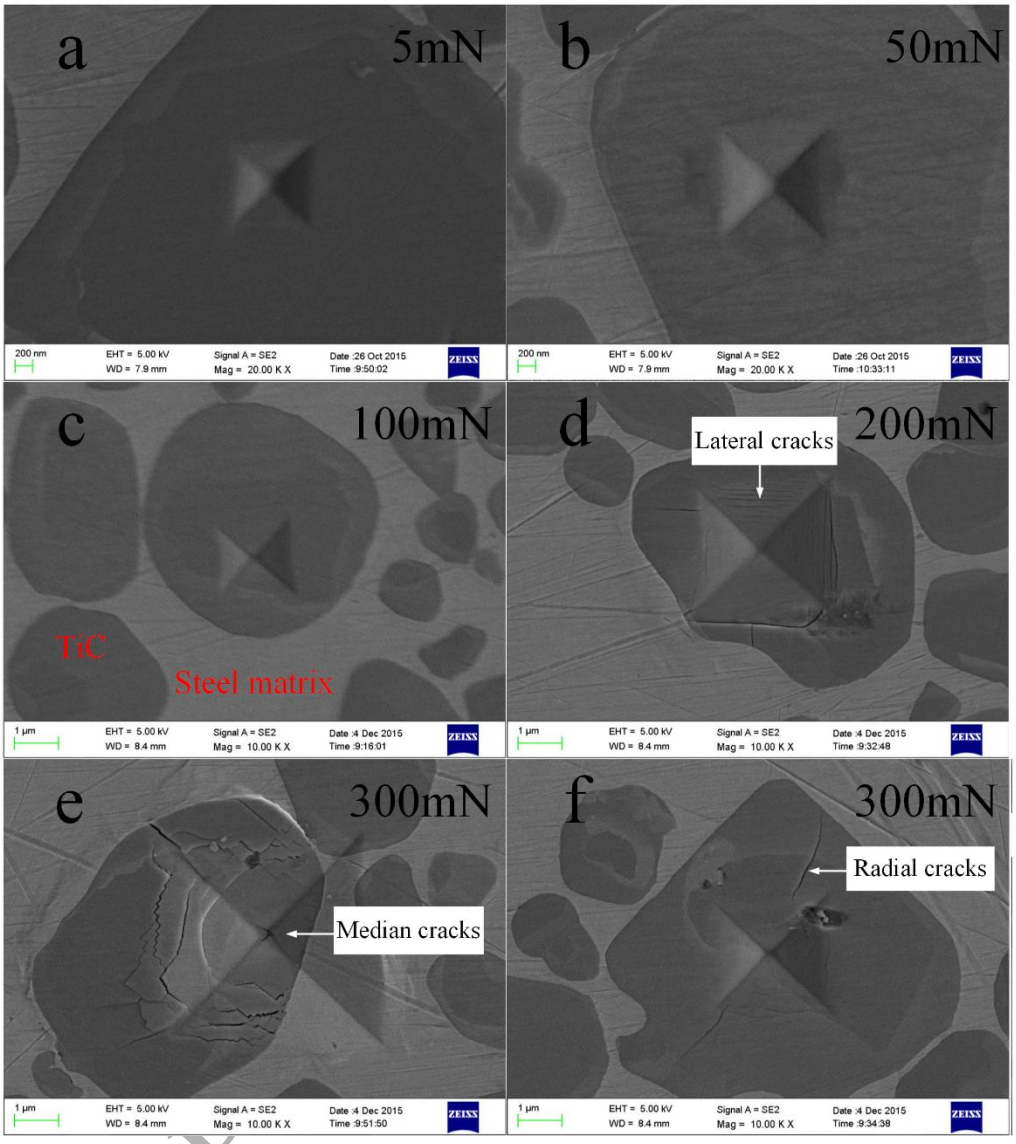

Fig. 10. SEM images vickers indentation topography for TiC particle at different loads of. (a) 5 mN. (b) 50 mN. (c) 100 mN. (d) 200 mN. (e) 300 mN (f) 300 mN.

The modulus and hardness of TiC particles by nanoindentation at different loads are shown in Fig. 11. It can be seen that the modulus and hardness increase with the increasing load when the load is below 50 mN. This is similar to the research outputs from Lee et al [24] of the inverse indentation size effect, which is due to the existence of indentor tip radii in Au

thin-film nanoindentations. Hwang et al. [25] proposed a model to explicate this phenomenon based on the MSG plasticity theory. It was found that the plastic deformation increases as the indenter tip radii increase, which causes the indentation hardness not to follow the indentation size effect under a smaller indentation depth. Then the modulus and hardness decrease when the load increases beyond 50 mN, which is consistent with the general indentation size effect (ISE)[26].

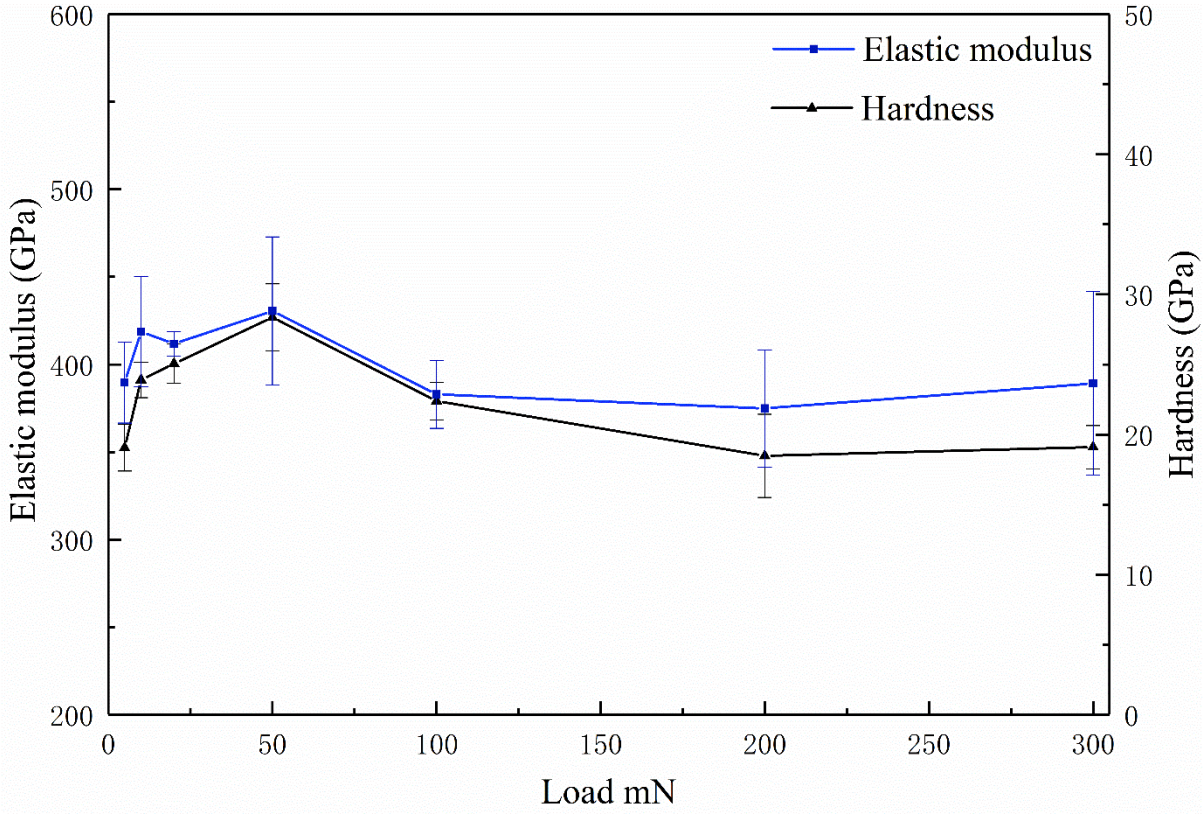

Fig. 11. Elastic modulus and hardness of TiC particle at different loads.

From Fig. 11, it can be concluded that the elastic modulus and hardness of the TiC particle under the ductile-brittle transition load are about 380 GPa and 20 GPa, respectively. These values are less than the elastic modulus (440GPa) and hardness (30 GPa) of single crystal TiC in literature[27]. This may be due to the matrix phase effects, as indicated in Fig.12. When the nanoindentation was applied on TiC particle, as shown in Fig. 12(b), the elastic

deformation of surrounding steel matrix occurred. The mismatch in material properties of the particle and matrix creates a secondary indentation effect, where the hard particle itself indents into the soft matrix. Hence, the depth of indentation is increased as compared with that of single crystal TiC in Fig. 12 (a), which results in the decreasing modulus and hardness. Therefore, the critical undeformed chip thickness h_{cr} of brittle-ductile transition during grinding GT35 will increase as compared with that of single crystal TiC, which can be obtained by [28],

$$h_{cr} = K_0 \cot(\frac{\alpha_0}{2})\sqrt{\frac{2\lambda_0}{\alpha}}\left(\frac{K_{Id}}{H}\right)^2 \quad (44)$$

where $K_0$is the affecting coefficient of the coolant, $K_0 = 1$[28]is applied here; α_0 is the top angle of indenter, $\alpha_0 \approx 120°$[28]; λ_0 is the integrative factor, $\lambda_0 = 1.6 \times 10^4$[28], α is the geometry factor of the indenter, $\alpha = 1.8854$;[28] and K_{Id} is the dynamic fracture toughness, $K_{Id} \approx 30\% K_{Ic}$, K_{Ic}=4.5 MPa $m^{1/2}$. According to Eq. (44), h_{cr} was approximately equal to 0.35 μm.

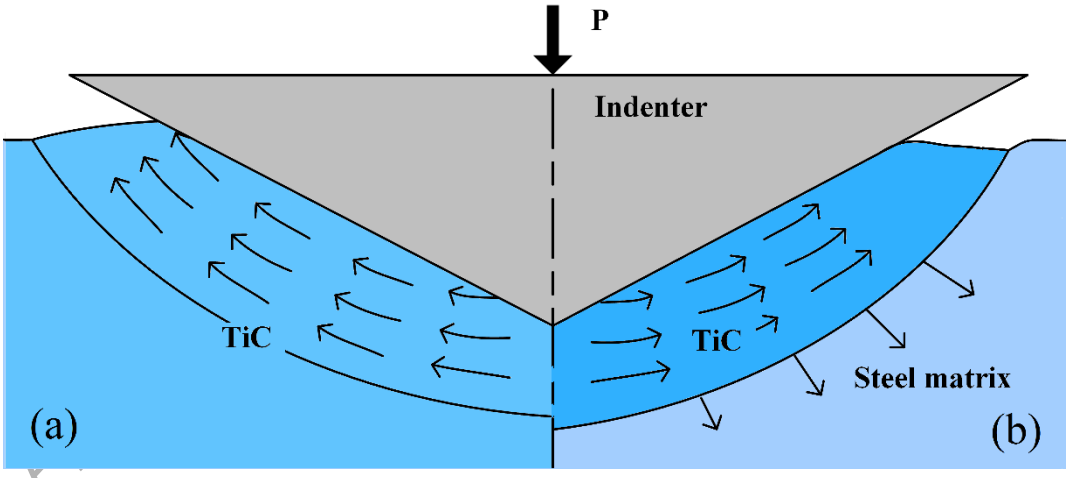

Fig. 12. Illustration of the effects of surrounding phases on the nanoindentation results. (a) Indentation on single crystal TiC. (b) Indentation on a TiC particle in GT35.

4.2 Material removal mechanisms of GT35 in grinding

SEM photographs of the typical surface morphologies of ground GT35 surface are shown in Fig. 13. Fig. 13 (a) shows that clear scratching marks on the steel matrix caused by abrasives are parallel to the feeding direction, so the material removal of the steel matrix was dominated by the ductile removal. When the abrasive grain ploughs the material surface, the steel matrix softens with increasing temperature because of the frictional contact between the grinding wheel and workpiece. The abrasive cutting edges were mapped at the machined surface to generate the grooves.

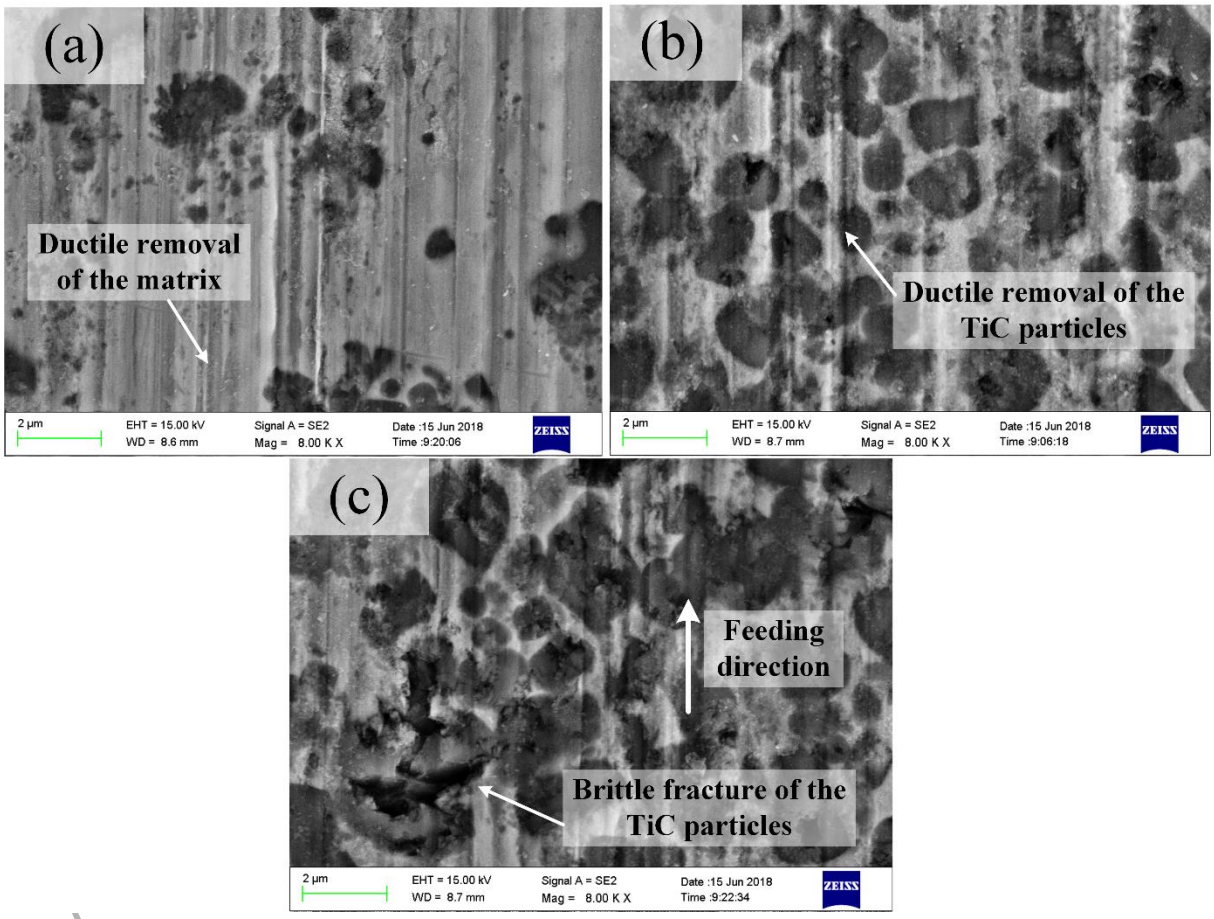

Fig. 13. Typical surface morphologies of GT35 after surface grinding with parameters of Δ=3 µm (a) v_w=0.113m/s v_s=15m/s (b) v_w=0.226m/s v_s=15m/s (c) v_w=0.226m/s v_s=10m/s

Fig. 13 (b) shows the SEM photograph of the ground surface with many TiC particles in steel matrix. The surface roughness Ra is 0.0456 μm. This figure clearly shows that most of the TiC particles have scratching marks along the feeding direction. It indicates that these TiC particles were removed in the ductile mode. Based on the results and discussion in the analysis of the cracking behaviors, the indentation fracture mechanics predicts a critical threshold depth below which lateral cracking should not occur. Hence, ductile grinding should prevail when the undeformed chip thickness is below this critical chip thickness and better surface quality can be achieved. Besides the ductile deformation of TiC particles, brittle removal and particle fractures were also observed in Figs. 13(b) and 13(c). More and deeper fractures can be found on the surface in Fig. 13(c) than in Fig. 13(b), which lead to a worse surface roughness of Ra 0.0746 μm in Fig. (c). Since the TiC particles is much harder than steel matrix, there is a sharp increase in the cutting force when the abrasive grains just cut into TiC particles, and shear on TiC particles at the interface of the two phases. When the forces of impact and shear approach fracture strength of TiC particles, microcrack is initiated, subsequent crack grows and propagate, the TiC particles are fragmented and fall off. In this stage, the brittle removal mode, which leads to the increase of surface roughness is reached.

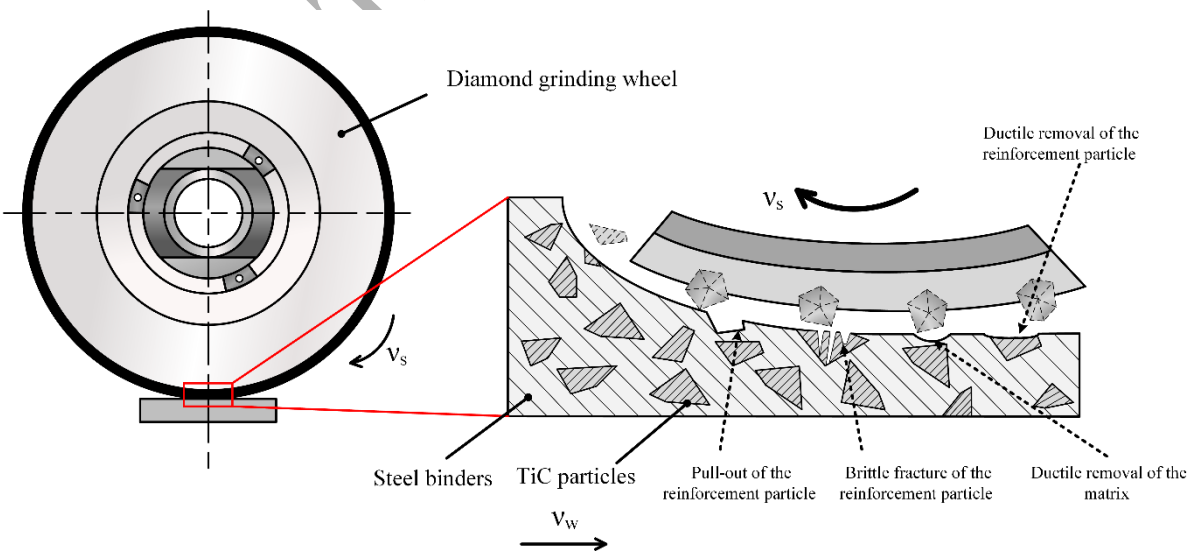

Fig. 14. Schematic of GT35 surface features produced in grinding.

The surface features of GT35 generated in grinding can be seen in a schematic view in Fig. 14. When the steel matrix is ground, it is removed in ductile regime. When the grains scratch the reinforcement particles, ductile mode removal takes place at small undeformed chip thickness. The smaller the maximum undeformed chip thickness is, the more TiC particles are ground in ductile mode. When undeformed chip thickness exceeds the critical value of the ductile-brittle transition, the brittle fracture occurs. In summary, the materials removal of GT35 during precision grinding consists of four stages: ductile removal of the matrix, ductile removal of the reinforcement particle, brittle fracture of the reinforcement particle and pull-out of the reinforcement particle. The higher proportion of TiC particles are ground in ductile mode, the better surface quality is generated.

4.3 Model validation

To validate the surface roughness model of PRMMCs in Eq. (38), single factor grinding experiments were conducted on the surface grinder, and their corresponding surface roughness values were measured. However, an adjustment factor involving groove overlapping, irregular grain shape, ploughing and contact deflection is necessary to correct the predictive values to the theoretical values, as:

$$E(R_a)_m = 0.8E(R_a) \tag{45}$$

The predicted surface roughness calculated by the novel and the traditional model [16] are compared with experimental surface roughness under different surface grinding conditions in Fig. 15. The results indicated that both the novel and traditional models are capable of capturing the trends of the surface roughness with varying grinding depth, workpiece speed and wheel speed. As shown in Fig. 15(a), it can be seen that the surface roughness decreased with the increase of wheel speed. This is due to the negative correlation between the wheel

speed and maximum undeformed chip thickness. Figs. 15(b) and15 (c) show the effects of both workpiece feed rate and grinding depth on the ground surface roughness. The surface roughness increases with the increase of feed rate and grinding depth. The observed trends might be due to the feed rate and grinding depth on the depth of engagement and thus resulting in a poor surface quality.

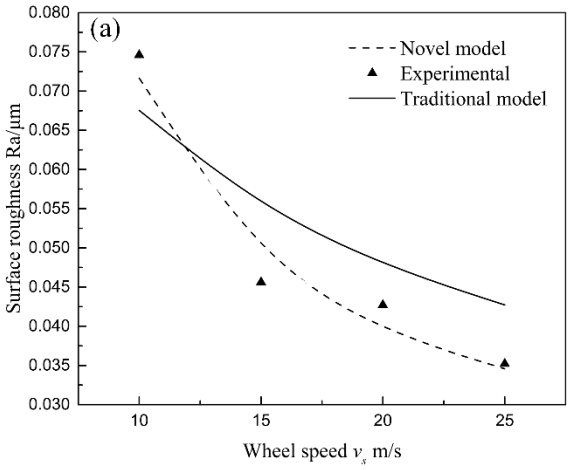

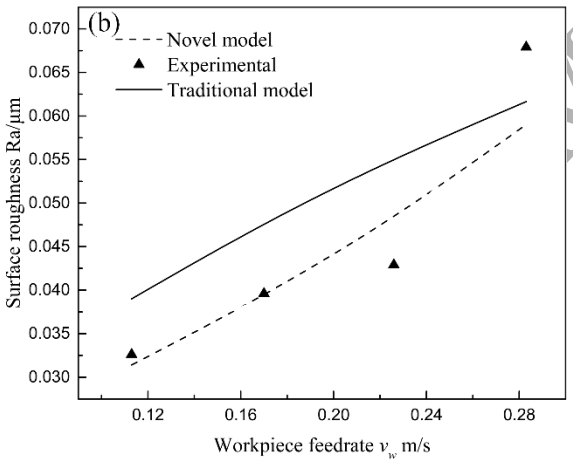

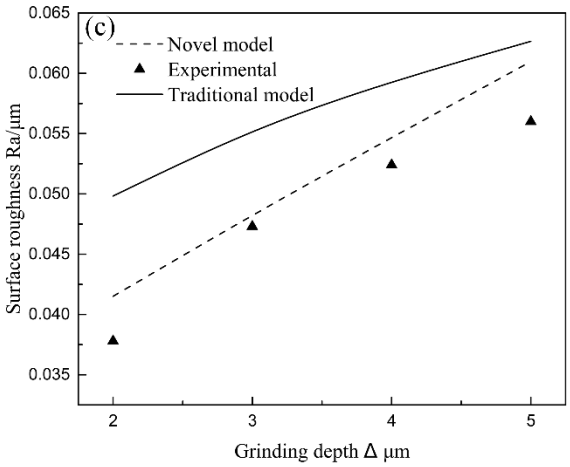

Fig. 15. Predicted and experimental surface roughness under different surface grinding conditions. (a) Δ=3μm v_w=0.226m/s (b) Δ=3μm v_s=15m/s (c) v_w=0.226m/s v_s=15m/s.

Furthermore, it is shown the difference of the average percentage of errors with prediction of 6.2 % in the novel model and 17.9 % for the traditional model of when compared with the experimental results. The traditional model over-estimates the surface roughness of GT35. By contrast, the novel analytical model in this study provides an overall more accurate estimation of surface roughness, and to some extent indicates the trend of surface roughness with input processing parameters. Thus, the novel model is more accurate than the traditional model in predicting surface roughness in precision grinding of PRMMCs. This is because the material removal mechanism of TiC particles transferring from ductile to brittle mode with the increasing maximum undeformed chip thickness is considered, while the traditional model neglected the different nanomechanical response between the matrix and reinforcements.

5 Conclusions

A novel analytical model for surface roughness prediction of precision ground PRMMCs was established and verified in this paper. The novelty of this model lies in integrating the combined nanomechanical responses of reinforcement particles and matrix material. The conclusions are summarized as follows:

(1) From the observations and measurements for ground GT35 surfaces, two phases in GT35 are removed in different mechanisms in grinding: the steel matrix is ground in ductile mode, and the TiC particles are ground by mixture of ductile mode and brittle mode. This results in ploughing striations and fracture areas occur at the same time.

(2) The nanoindentation results of the steel matrix and TiC particles help to understand the material removal mechanism of GT35. The nanoindentation tests of TiC particle in GT35

indicated that the overall modulus and hardness of the TiC particle with its surrounding steel matrix is reduced from that of TiC itself. This is due to the secondary indentation of TiC in the surrounding steel matrix. The critical undeformed chip thickness for the transition of ductile mode to brittle mode for GT35 is determined.

(3) An analytical surface roughness prediction model of ground PRMMCs considering different removal mechanisms of matrix and reinforcements was proposed. Results obtained from this model correlate well with the experimental results with an average error of 6.2 % for precision grinding of GT35 with various grinding parameters. This model is helpful for determining optimized grinding parameters.

Acknowledgements

This work was supported by National Key R&D Program of China (No. 2017YFB1301900), National Natural Science Foundation of China (No. 51875321), Shandong Provincial Natural Science Foundation (No. ZR2018MEE019) and Major Basic Research of Shandong Provincial Natural Science Foundation (No. ZR2018ZB0521).

References

[1] Duan C, Sun W, Fu C, Zhang F. Modeling and simulation of tool-chip interface friction in cutting Al/SiCp composites based on a three-phase friction model. Int J Mech Sci.2018; 142–143(384-396).

[2] Ghandehariun A, Kishawy H, Balazinski M. On machining modeling of metal matrix composites: A novel comprehensive constitutive equation. Int J Mech Sci.2016; 107(235-241).

[3] Tomita Y, Higa Y, Fujimoto T. Modeling and estimation of deformation behavior of particle-reinforced metal-matrix composite. Int J Mech Sci.2000; 42(11):2249-2260.

[4] Wang Z, Lin T, He X, Shao H, Tang B, Qu X. Fabrication and properties of the TiC reinforced high-strength steel matrix composite. Int J Refract Met Hard Mater 2016; 58: 14-21.

[5] Li HN, Yu TB, Da Zhu L, Wang WS. Analytical modeling of ground surface topography in monocrystalline silicon grinding considering the ductile-regime effect. Arch Civ Mech Eng 2017;17: 880-893.

[6] Huang H, Liu YC. Experimental investigations of machining characteristics and removal mechanisms of advanced ceramics in high speed deep grinding. Int J Mach Tools Manuf 2003; 43: 811-823.

[7] Li Z, Zhang F, Luo X. Subsurface damages beneath fracture pits of reaction-bonded silicon carbide after ultra-precision grinding. Appl Surf Sci 2018;448: 341-350.

[8] Wang W, Yao P, Wang J, Huang C, Zhu H, Zou B, Liu H, Yan J. Crack-free ductile mode grinding of fused silica under controllable dry grinding conditions. Int J Mach Tools Manuf 2016;109: 126-136.

[9] Hung NP, Zhong ZW. Ductile Regime Machining of Metal Matrix Composites. Mach Sci Technol 1999; 3:255-271.

[10] Yu X, Huang S, Xu L. ELID grinding characteristics of SiCp/Al composites. Int J Adv Manuf Technol 2016; 86: 1165-1171.

[11] Xi X, Ding W, Li Z, Xu J. High speed grinding of particulate reinforced titanium matrix composites using a monolayer brazed cubic boron nitride wheel. Int J Adv Manuf Technol 2017; 90: 1529-1538.

[12] Liu C, Ding W, Yu T, Yang C. Materials removal mechanism in high-speed grinding of particulate reinforced titanium matrix composites. Prec Eng 2018; 51: 68-77.

[13] Basheer AC, Dabade UA, Joshi SS, Bhanuprasad VV, Gadre VM Modeling of surface roughness in precision machining of metal matrix composites using ANN. J Mater Process Technol 2008;197: 439-444.

[14] Kwak JS, Kim YS. Mechanical properties and grinding performance on aluminum-based metal matrix composites. J Mater Process Technol 2008; 201: 596-600.

[15] Chandrasekaran M. Artificial neural network modeling for surface roughness prediction in cylindrical grinding of Al-SiCp metal matrix composites and ANOVA analysis. Adv Prod Eng Manag 2014; 9: 59-70.

[16] Hecker RL, Liang SY. Predictive modeling of surface roughness in grinding. Int J Mach Tool Manuf 2003; 43: 755-761.

[17] Agarwal S, Rao PV. A new surface roughness prediction model for ceramic grinding. P I Mech Eng B-J Eng Manuf 2005; 219: 811-821.

[18] Matsumoto M, Huang H, Harada H, Kakimoto K, Yan J. On the phase transformation of single-crystal 4H–SiC during nanoindentation. J Phy D: Appl Phys 2017; 50: 265-303.

[19] Younis MA, Alawi H. Probabilistic analysis of the surface grinding process. T Can Soc Mech Eng 1984; 8: 208-213.

[20] Zheng F, Kang R, Dong Z, Guo J, Liu J, Zhang J. A theoretical and experimental investigation on ultrasonic assisted grinding from the single-grain aspect. Int J Mech

Sci.2018; 148:667-75.

[21] Jing X, Maiti S, Subhash GA. New Analytical Model for Estimation of Scratch-Induced Damage in Brittle Solids. J Am Ceram Soc 2007; 90: 885-892.

[22] Gu W, Yao Z, Li K. Evaluation of subsurface crack depth during scratch test for optical glass BK7. P I Mech Eng C-J Mec 2011; 225: 2767-2774.

[23] Arif M, Rahman M, San WY. Analytical model to determine the critical feed per edge for ductile–brittle transition in milling process of brittle materials. Int J Mach Tool Manu 2011; 51: 170-181.

[24] Lee Y, Kim Y, Hahn J. Hardness Variation with Indenter Sharpness in an Au Thin-Film. J Nanosci Nanotechno 2012; 12:5648-52.

[25] Hwang KC, Huang Y, Li M, Xue Z. The Influence of Indenter Tip Radius on the Micro-Indentation Hardness. J Eng Mater Technol 2002; 124: 371-379.

[26] Peng Z, Gong J, Miao H. On the description of indentation size effect in hardness testing for ceramics: Analysis of the nanoindentation data. J Eur Ceram Soc 2004; 24: 2193-2201.

[27] Maerky C, Guillou MO, Henshall JL, Hooper RM. Indentation hardness and fracture toughness in single crystal TiC 0.96. Mater Sci Eng A-Struct 1996; 209: 329-336.

[28] Chen M, Zhao Q, Dong S, Li D. The critical conditions of brittle–ductile transition and the factors influencing the surface quality of brittle materials in ultra-precision grinding. J Mater Process Technol 2005; 168: 75-82.